IOPscience iopscience.iop.org

Home Search Collections Journals About Contact us My IOPscience

Structural characterization of thin layered materials using x-ray standing wave enhanced elastic and inelastic scattering measurements

This article has been downloaded from IOPscience. Please scroll down to see the full text article.

2010 J. Phys.: Condens. Matter 22 175003

(http://iopscience.iop.org/0953-8984/22/17/175003)

View the table of contents for this issue, or go to the journal homepage for more

Download details:
IP Address: 129.252.86.83
The article was downloaded on 30/05/2010 at 07:52

Please note that terms and conditions apply.

IOP PUBLISHING JOURNAL OF PHYSICS: CONDENSED MATTER
J. Phys.: Condens. Matter **22** (2010) 175003 (8pp) doi:10.1088/0953-8984/22/17/175003

Structural characterization of thin layered materials using x-ray standing wave enhanced elastic and inelastic scattering measurements

M K Tiwari[1,2] **and K J S Sawhney**[1]

[1] Diamond Light Source Ltd, Harwell Science and Innovation Campus, Didcot, Oxfordshire OX11 0DE, UK
[2] Indus Synchrotron Utilization Division, Raja Ramanna Center for Advanced Technology, Indore 452013, India

Received 4 January 2010, in final form 26 February 2010
Published 29 March 2010
Online at stacks.iop.org/JPhysCM/22/175003

Abstract
By measuring the intensities of the x-ray standing wave induced elastic and inelastic x-ray scattering from thin multilayer structures, we show that structural characterizations of the high and low z (atomic number) material layers can be performed independently. The method has been tested by analyzing the structural properties of an Nb/C/Nb trilayer and an Mo/Si periodic multilayer structure. The results of the x-ray scattering measurements have been compared with those obtained using x-ray reflectivity and conventional x-ray standing wave fluorescence techniques. It has been demonstrated that the present approach is especially suitable for studying multilayer structures comprising low atomic number layers, as it eliminates the requirement of a fluorescence signal, which is very weak in the case of low z materials.

(Some figures in this article are in colour only in the electronic version)

1. Introduction

Interaction of x-rays with matter takes place by various ways such as photoelectric absorption, elastic and inelastic (Compton) scattering, and electron–hole pair production. These processes often lead to the production of different types of secondary x-rays such as fluorescent, coherent and Compton x-rays, and different types of electrons namely photoelectrons, Auger electrons and Compton recoil electrons. The properties of a material are usually characterized by measuring one or more of these secondary electrons and x-rays. Multilayer structures composed of thin layers of alternating high and low z materials [1, 2] have a wide range of applications in many fields. Such structures offer unique structural [3], magnetic [4, 5] and electronic [6, 7] properties. The microstructural properties such as layer thickness, interface roughness, interlayer formation etc of the layered materials is usually determined from the x-ray reflectivity (XRR) [8], x-ray diffuse scattering [9] and from the x-ray standing wave (XSW) induced fluorescence measurements [10–15]. The XRR technique, in combination with the x-ray diffuse scattering measurements, has shown to be a very powerful technique for the determination of correlated and un-correlated (random) interfacial roughness effects in a multilayer stack [16–18]. The XRR technique however has the limitation that it does not provide any element-specific information. Moreover, it only gives the composite thickness and roughness for the high and low z layers of the periodic multilayer structures, and sometimes it becomes rather difficult to establish the true microstructural parameters of the multilayer structures.

XSW induced fluorescence measurement is a more direct method to determine the structural properties of high z layers in the periodic multilayer structures. The fluorescence signal from the low z layer is weak due to its low fluorescence yield and the strong self-absorption in the layered material. Therefore, the structural information of the low z layers is determined indirectly from the XSW fluorescence measurement of the high z layers. The scattered x-ray intensities (elastic and Compton) emitted from a thin layered material also contain the information about structural parameters of the thin film system. In practice, however, it is very difficult to retrieve such information.

 © 2010 IOP Publishing Ltd Printed in the UK & the USA

In literature, no direct formulation has been provided to determine the structural properties of the layered materials using XSW enhanced elastic and Compton scattered x-rays. In some applications, it is important to determine the layer properties of the individual layers, for example, in x-ray wave guide structures (trilayers) where a thick low z layer is sandwiched between two high z layers. The microstructural characterization of a multilayer structure using XSW induced fluorescence measurements has been described by several workers [10–12]. Only a few research groups [19, 20] have reported the XSW enhanced x-ray scattering measurements from the multilayer structures with an aim to determine the amorphous or crystalline properties and to measure the diffuse scattered intensities, from the interface of the two layer media. They however have only investigated the elastically scattered x-ray intensities from a multilayer structure.

We report here XSW characterization of thin layered materials using elastic and Compton scattered x-ray intensities. The underlying theoretical formulism is described and is used for simulating grazing incidence angle dependent elastic and Compton scattered intensity profiles from different types of thin multilayer structures. Two repetitive multilayer structures Nb/C/Nb trilayer structure and Mo/Si periodic multilayer structure have been analyzed. The results of simulations then compared with experimental measurements using synchrotron x-rays. The XSW enhanced elastic x-ray scattering profile from a multilayer material is largely sensitive to the x-ray scattering cross section of high z layers, whereas the Compton scattering profile is more sensitive to the x-ray scattering cross section of low z layers. We used this property to correlate the structural properties of high and low z layers with their measured XSW enhanced elastic and Compton scattering profiles. Unlike conventional XSW fluorescence measurements, the method proposed by us has the advantage that one is able to determine the information on both high and low z layers independently. Moreover, measurement of several XSW profiles (elastic, Compton and fluorescence) provides greater accuracy in evaluating the microstructural properties of the thin film structures.

2. Theoretical background

To determine the angle dependent elastic and inelastic scattered x-ray intensity profiles from a layered structure, explicit knowledge of electromagnetic x-ray field intensity distribution at each point of the layer medium is needed. In the literature, several methods [10–12] are known which describe the calculation of net x-ray field intensity inside a layered medium. We have followed the recursive methodology [10].

The normalized x-ray field intensity $I_j(\theta, Z)$ in layer j of a multilayer structure consisting of n layers, at depth Z is given by [15]

$$I_j(\theta, Z) = \frac{|E_j^{\mathrm{i}} + E_j^{\mathrm{r}}|^2}{|E_j^{\mathrm{i}}|^2} = \left\{\exp(-2k''_{j,z}Z) + \left|\frac{E_j^{\mathrm{r}}}{E_j^{\mathrm{i}}}\right|^2 \times \exp(2k''_{j,z}Z) + 2\left|\frac{E_j^{\mathrm{r}}}{E_j^{\mathrm{i}}}\right| \cos[\nu(\theta) + 2k'_{j,z}Z]\right\} \quad (1)$$

where E_j^{i} and E_j^{r} are the electromagnetic field amplitudes at the top of the layer j. $k'_{j,z}$ and $k''_{j,z}$ represent the real and imaginary part of the z-component of wavevector k. The component of wavevector k in the jth layer can be written as

$$k_{j,x} = \frac{2\pi}{\lambda}\cos\theta, \qquad k_{j,z} = \frac{2\pi}{\lambda}(\varepsilon_j - \cos^2\theta)^{1/2}$$

where $\varepsilon_j = 1 - 2\delta_j - \mathrm{i}2\beta_j$ is the complex dielectric constant of medium j. λ is the wavelength of incident radiation. δ_j and β_j are the optical constants of the jth medium. $\nu(\theta)$ is the phase of the E-field ratio and given by

$$\frac{E_j^{\mathrm{r}}}{E_j^{t}} = \left|\frac{E_j^{\mathrm{r}}}{E_j^{t}}\right| \times \mathrm{e}^{\mathrm{i}\nu(\theta)}.$$

The net elastically scattered intensity, Compton scattered intensity and x-ray fluorescence intensity, emitted from the jth layer of a multilayer structure can be evaluated using the following relations

$$I_j^{\mathrm{elastic}}(\theta) \propto \sigma_{\mathrm{elastic}}(E_0) \int_0^d I_j(\theta, Z) \times \exp\left[-\left(\frac{(\mu/\rho)_{E_0}}{\sin\varphi}\right)\rho Z\right] \mathrm{d}Z \quad (2)$$

$$I_j^{\mathrm{Compton}}(\theta) \propto \sigma_{\mathrm{Compton}}(E_0) \int_0^d I_j(\theta, Z) \times \int \mathrm{d}E \exp\left[-\left(\frac{(\mu/\rho)_{E}}{\sin\varphi}\right)\rho Z\right] \mathrm{d}Z \quad (3)$$

$$I_j^{\mathrm{fluo}}(\theta) \propto \tau(E_0) \int_0^d I_j(\theta, Z) \times \exp\left[-\left(\frac{(\mu/\rho)_{E_{\mathrm{char}}}}{\sin\varphi}\right)\rho Z\right] \mathrm{d}Z \quad (4)$$

where d is the thickness of the jth layer and ρ is the density of layer j in g cm^{-3}. $\sigma_{\mathrm{elastic}}$, $\sigma_{\mathrm{Compton}}$ and τ are the elastic, Compton and photoelectric x-ray cross sections of the jth layer element at incident x-ray energy of E_0. These x-ray cross sections largely depend on the atomic number (z) of the material (for example: $\tau_{\mathrm{photo}} \propto z^4$, $\sigma_{\mathrm{elastic}} \propto z^2$, and $\sigma_{\mathrm{Compton}} \propto z$) and their values can be evaluated from the McMaster and Hubbell tables [21, 22]. Also, there are many software packages [23–25], which can be used to calculate the x-ray cross sections (in cm^2 g^{-1}) of different materials at various x-ray energies. $(\mu/\rho)_{E_0}(\mu/\rho)_{E_{\mathrm{char}}}$ and $(\mu/\rho)_E$ respectively represent the mass attenuation coefficient in cm^2 g^{-1} for layer j at excitation energy E_0, emitted characteristic energy E_{char}, and at mean scattered x-ray energy of E. φ is the takeoff angle for the emitted and scattered x-rays from the multilayer surface ($\varphi \sim 90°$). dE is the observed energy spread of the Compton scattered x-rays from the mean energy E, for an scattering angle of φ.

The total elastic or Compton scattered x-ray intensity from a multilayer structure can be obtained by summing the contribution from all layers including the Si substrate, and taking into account the absorption correction of the upper layers. The scattering contribution from the Si substrate adds a fixed background to the elastic as well as the Compton scattering profiles, which has been taken into account in the

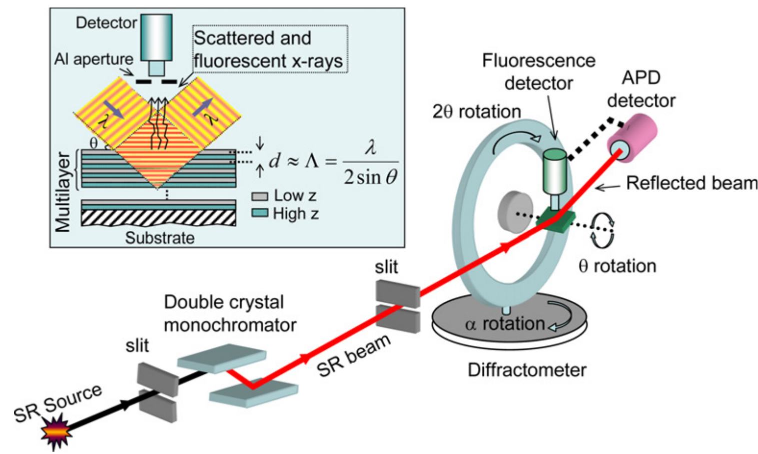

Figure 1. A schematic arrangement of the experimental setup used for XSW induced fluorescence excitation and x-ray scattering measurements on B16 beamline at the Diamond Light Source, UK [26]. The inset shows an illustration of the principle of the XSW field excitation in a multilayer structure.

calculations. The substrate scattering contribution does not modify or alter the structural information derived from the measured elastic or Compton scattering profiles.

3. Experimental details

Grazing incidence angle dependent elastic and Compton x-ray scattering measurements of the multilayer structures were carried out on the B16 Test beamline at Diamond Light Source [26]. X-ray energies in the range of 15–17 keV, monochromatized from a Si(111) double crystal monochromator were used to excite Nb/C/Nb trilayer and Mo/Si multilayer structures, at grazing incidence angles. The measurements were carried out in top-up operation mode of diamond, at a ring current of 250 mA. The XSW and XRR measurements of the multilayer samples were performed on a five-axis Huber diffractometer in θ–2θ geometry, in the ambient air environment. Figure 1 shows the schematic arrangement of the experimental setup used for XSW induced fluorescence and x-ray scattering measurements. The multilayer samples were mounted on the sample stage of diffractometer, which consist of three (XYZ) precision motorized stages. These stages facilitate the alignment of the thin film samples with accuracies better than 1 μm. We also employed an optical microscope for preliminary visual alignment of the samples however the final alignment were done using x-rays. The measured ‘sphere of confusion’ (SOC) of the diffractometer station over the full range of all 5-axis, with a sample load of 20 kg, was found to be better than 60 μm. Fluorescent and scattered x-ray intensities emitted from the multilayer samples were dispersed and collected by a Vortex energy dispersive spectroscopy detector, placed normal to the sample surface. A 2 mm Al collimator was used between the sample and detector to maintain a constant solid angle of detection on the sample surface, at various incidence angles. The fluorescence measurements were taken for an acquisition live time of 30 s at each angular position of the sample. To measure the specular reflected x-ray intensities from the sample, an avalanche photodiode detector (APD), capable of measuring very high count rates and having a large dynamic range, was used. The multilayer structures were fabricated using a DC magnetron sputtering system in argon atmosphere with a deposition rate of $\sim$5 Å min^{-1}. The details of the deposition system are given elsewhere [27]. The thin film structures were deposited on the Si(100) substrate, which was kept at room temperature. Before deposition, the rms roughness of the Si substrates was characterized in detail using a laboratory source x-ray reflectometer and was found to be $\sim$5 $\pm$ 1 Å.

4. Examples of calculation of elastic scattering, Compton scattering and fluorescence profiles from multilayer structures

4.1. Nb/C/Nb trilayer structure

For a simple case, we have considered a trilayer structure, where a low z layer (carbon) is sandwiched between two high z (niobium) layers. Figure 2(a) gives the contour plot of x-ray field intensity distribution (equation (1)) inside the Nb (6 nm)/C (30 nm)/Nb (25 nm) trilayer structure, calculated at an incident x-ray energy of 17 keV, as a function of incidence angle and depth Z in the layer medium. From figure 2(a), it can be seen that various transverse electric field modes (TE_0, TE_1, TE_2, etc) are excited in the C layer medium at definite incidence angles. At large incidence angles (for higher modes), the x-ray field intensity moves towards the interfaces of the layered medium, thus provides a possibility to determine the interface properties of the high and low z layers by measuring the fluorescence or scattered intensities from the layered medium. The scattering and photoelectric x-ray cross sections depend on x-ray energy and on the element species. The variation of various x-ray cross sections as a function of x-ray energy, for Nb and C elements is shown in figure 2(b). These x-ray cross sections have been calculated using XOP software package [23]. It can be seen that different cross

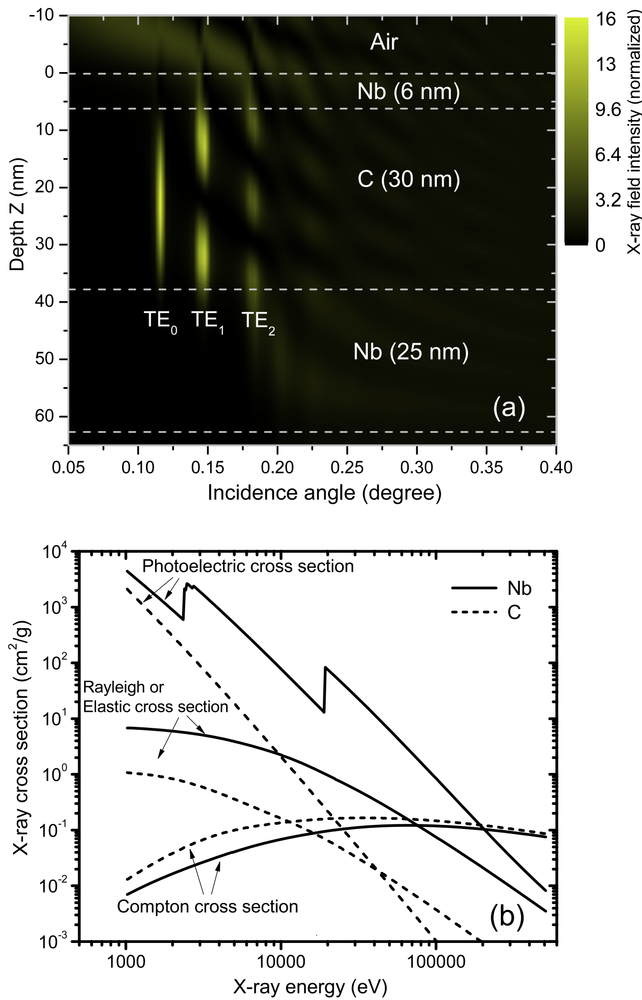

Figure 2. (a) Contour plot of x-ray field intensity distribution inside an Nb (6 nm)/C (30 nm)/Nb (25 nm) trilayer structure as a function of incidence angle and the depth Z in the layer medium, at x-ray energy of 17 keV. From this figure it can be seen that various transverse electric field modes (TE_0, TE_1, TE_2, etc) are excited in the C layer at definite incidence angles. (b) Variation of the elastic, Compton and photoelectric x-ray cross sections of Nb and C elements as a function of incident x-ray energy. From this figure, it can be seen that at a given x-ray energy the different x-ray cross sections are largely sensitive to an element species.

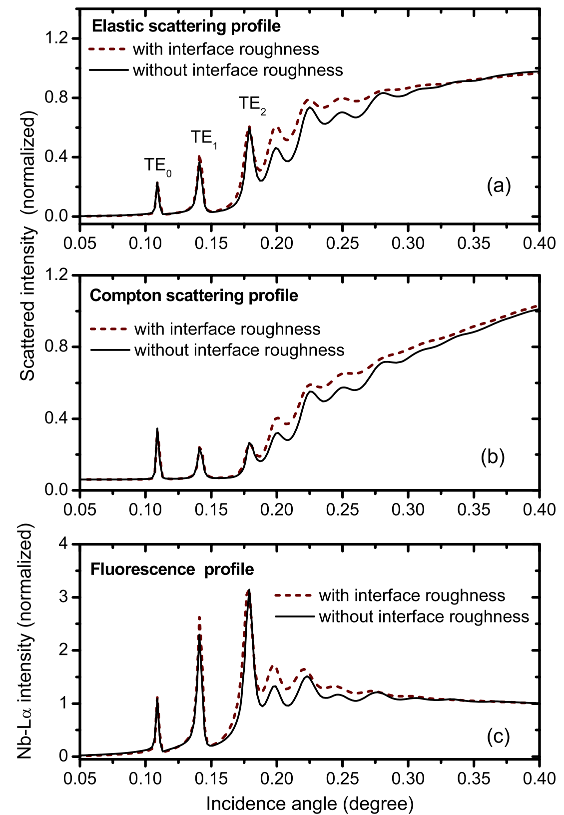

Figure 3. Calculated grazing incidence angle dependent x-ray scattering and fluorescence profiles for Nb (6 nm)/C (30 nm)/Nb (25 nm) trilayer structure using equations (2)–(4). (a) Elastic scattering, (b) Compton scattering, and (c) x-ray fluorescence profile of the Nb Lα line. All the profiles have been normalized at incidence angle of 0.4°.

sections have strong photon energy dependence, and also a z-dependence. The figure shows that one can get enough contrast of different x-ray cross sections between high z (niobium) and low z (carbon) materials.

Figure 3 depicts the calculated (using equations (2)–(4)) angle dependent elastic, Compton and x-ray fluorescence profiles of the Nb (6 nm)/C (30 nm)/Nb (25 nm) trilayer structure. The solid lines show the calculations performed assuming ideal interface properties (i.e. no interlayer roughness between different layers) whereas the dashed lines show the simulations for the case of non-ideal interfaces. For the latter, typical interface roughness values of $\sigma_{\mathrm{C\ layer}} = 1.0$ nm, $\sigma_{\mathrm{Top\ Nb\ layer}} = 2.0$ nm and $\sigma_{\mathrm{Bottom\ Nb\ layer}} = 1.0$ nm, have been used. Figures 3(a) and (b), show the variation of elastic and Compton scattered x-ray intensities as a function of grazing incidence angles. It can be seen from these curves that the profiles are quite sensitive to the interlayer roughness. The figures further show that the elastic and Compton scattering profiles differ from each other quite significantly, especially at incidence angles below the critical angle of the Nb layers ($\theta_c \sim 0.18°$). Several peaks corresponding to TE_0, TE_1, TE_2, etc modes appear in the calculated profiles below θ_c. These peaks occur due to the formation of XSW field in the Nb/C/Nb trilayer medium. The height of these peaks strongly depends on the XSW field intensity distribution inside the trilayer medium as well as on the structural properties of the high and low z layers. Figure 3(c) demonstrates the calculated angle dependent Nb Lα fluorescence profile, observed from the Nb layers. It can be seen from figures 3(a) and (c) (cf figures 3(a) and (c)), that the nature of the elastic and Nb Lα fluorescence profiles is very well correlated especially in the incidence angle range below θ_c of Nb. These calculations show that the angle dependent profiles of different scattered photons (elastic, Compton and fluorescent x-rays) emitted from thin layered materials, are primarily sensitive to the atomic numbers of the constitute layers (high z and low z layers). The elastically x-ray scattered x-rays mainly originate from the high z layers while the Compton scattered x-rays mostly originate from the low z layers. Because, at a given x-ray energy, the elastic x-ray cross section ($\sigma_{\mathrm{elastic}} \propto z^2$) and Compton x-ray cross section ($\sigma_{\mathrm{Compton}} \propto z$) strongly depend on the atomic number of a

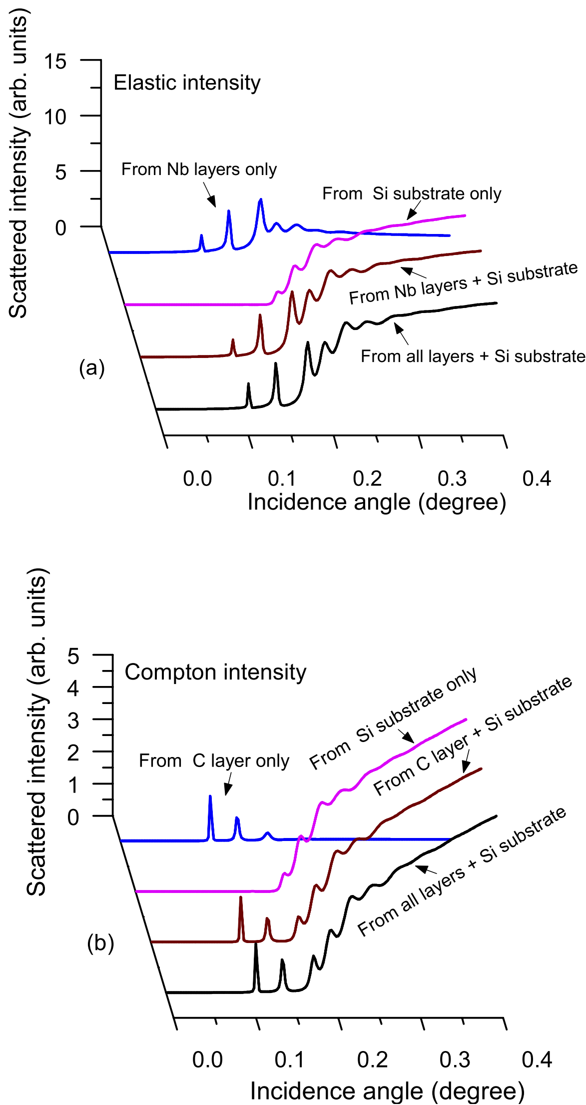

Figure 4. Calculated grazing incidence angle dependent x-ray scattering profiles of the Nb/C/Nb trilayer structure, showing the scattering contribution arising from the different layers and from the Si substrate. (a) Elastic scattering, and (b) Compton scattering.

material. The angle dependent XSW enhanced measurements of elastic and Compton x-ray scattering intensities from a thin film medium therefore enable determination of structural properties of both high and low z layers separately.

In figures 4(a) and (b), we have presented the calculations for scattering contribution arising from the different high or low z layers, and also from the Si substrate, to the net elastic and Compton scattering intensity observed from an Nb/C/Nb trilayer structure. In order to calculate the scattering contribution from the Si substrate, we have considered infinite thickness of the Si substrate. The calculations show that the substrate scattering only adds a fixed background to the angle dependent elastic and Compton scattering profiles. It does not modify the nature of the peaks in the scattering profiles that originate from the Nb/C/Nb medium. It can also be seen from figures 4(a) and (b) that the total elastic and Compton scattering intensity appearing from the Nb/C/Nb trilayer structure strongly depend on the structural properties of the high and low z layers, respectively.

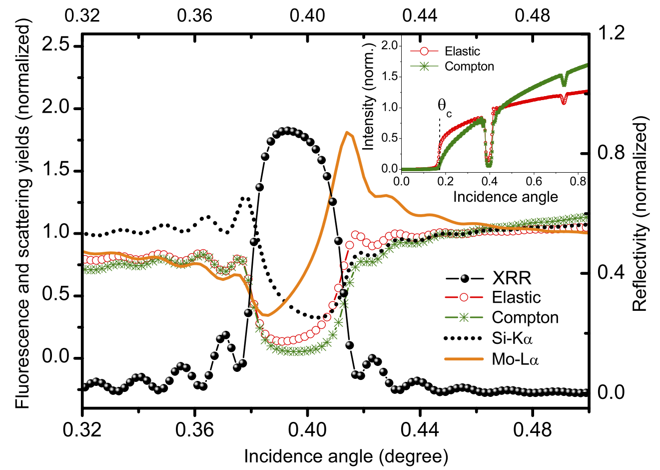

Figure 5. Calculated grazing incidence angle dependent elastic, Compton scattering and fluorescence profiles of a Mo/Si multilayer structure ($d = 6.6$ nm, structure factor (Γ) $= 0.36$, $N = 20$ layer pairs) in the vicinity of first Bragg order. Incident x-ray energy of 15.0 keV was used as excitation energy in these calculations. In this figure, we have also plotted the calculated XRR profile of the multilayer across the Bragg region. In the inset calculated elastic, Compton scattering profiles are shown over the large incidence angle range.

4.2. Mo/Si periodic multilayer structure

We have also performed calculations for the XSW enhanced Compton and elastic scattering from a periodic multilayer structure. Figure 5 shows the calculated elastic, Compton and fluorescence profiles for a Mo/Si ($d = 6.6$ nm, structure factor (Γ) $= 0.36$, $N = 20$ layer pairs) periodic multilayer structure, deposited on a Si substrate. In this figure, the normalized elastic, Compton and fluorescence yields have been plotted as a function of incidence angle in the vicinity of first Bragg order. All the profiles are normalized at high incidence angle of $\theta = 0.45°$. In this figure, we have also shown calculated XRR profile across the Bragg region. It can be seen from figure 5 that the fluorescence yield of Si Kα is higher at low angle side of the Bragg peak on the other hand fluorescence yield of Mo Lα attains its maximum value at the higher angle side of the Bragg peak. The calculated elastic scattering profile also demonstrates the similar behavior like the Mo Lα fluorescence profile. The elastic scattering yield increases at higher angle side of the Bragg peak because in this the condition the position of XSW antinodes coincides with the position of the Mo layers inside the multilayer structure and as a result one observes an increased elastic scattering yield from the Mo layers. This shows that using elastic scattering profile it should be possible to determine the structural properties of high z layers (Mo layers) in a similar approach like one gets using XSW fluorescence measurements from the high z layers. On the other hand, the Compton scattering yield decreases at the higher angle side of the Bragg peak because the Compton scattering cross section reduces from the high z layers. From figure 5, it can be seen that two x-ray scattering profiles (elastic

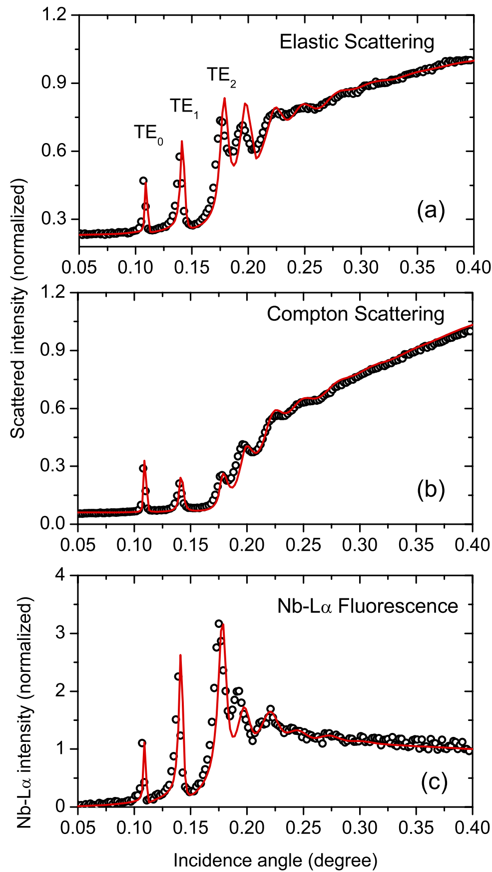

Figure 6. Measured elastic, Compton, and Nb Lα fluorescence profiles from an Nb/C/Nb trilayer structure. The scattered points show the experimental data while solid lines show the best fits to the measured profiles.

and Compton) are clearly distinguishable at the higher angle side of the Bragg peak. In the inset of figure 5, we have also shown the calculated elastic and Compton scattering of the Mo/Si multilayer structure for a large incidence angle range. It can be seen from this figure, that the Compton and elastic scattering profiles are also significantly different in the vicinity of critical angle (θ_c) of the multilayer structure.

5. Results and discussion

Figure 6 shows the measured and fitted elastic, Compton and x-ray fluorescence profiles of the Nb/C/Nb trilayer structure. From figures 6(a) and (b), it can be seen that the relative peak height ratios of the TE_0, TE_1 and TE_2 modes are quite different in the measured angle dependent elastic and Compton profiles. This ratio strongly depends on the thickness ratios of the high and low z layers. At large incidence angles, the higher transverse electric field modes (i.e. TE_1, TE_2, etc) move towards the top and bottom Nb cladding layers (see figure 2). As a result, the peak intensity of these modes increases in the measured elastic scattering profile while inversely it decreases in the measured Compton profile. The Compton scattered intensity for higher electric field modes decreases because the effective amount of XSW intensity contained in the low z medium (carbon layer) decreases. Figure 6(c)

Table 1. Structural parameters of the Nb/C/Nb trilayer structure determined from the combined analysis of grazing incidence angle dependent elastic scattering, Compton scattering, and Nb Lα fluorescence measurements.

# Layer name	Measured structural parameters of Nb/C/Nb trilayer structure	
	Thickness (nm)	rms roughness σ (nm)
Top Nb layer	6.5 ± 0.1	2.5 ± 0.2
C layer	30.7 ± 0.3	0.8 ± 0.1
Bottom Nb layer	24.9 ± 0.3	1.2 ± 0.2
Si-oxide layer (between bottom Nb layer and Si substrate)	2.5 ± 0.5	0.4 ± 0.2

shows measured and fitted Nb Lα fluorescence profiles for the NB/C/Nb trilayer structure. From figures 6(a) and (c), it can be seen that the measured elastic scattering and fluorescence profiles show more or less similar behavior. The Compton scattering contribution arises largely from the low z material in a layered medium, hence the Compton scattering profile offers a more accurate determination of structural properties of the C layer. On the other hand, elastic and Nb Lα fluorescence profiles originate from the high z layers and therefore facilitate precise determination of structural parameters of the Nb layers. The technique offers the advantage that by controlling the incidence angle, one can control the depth of the standing wavefield pattern, and hence the probed depth inside any thin film medium. On the other hand, the photon energy of the detected x-ray radiation (elastic and Compton scattered as well as fluorescent x-rays) provides elemental sensitivity. This independent control of spatial and elemental sensitivity makes the technique a powerful material characterization tool.

By analyzing all the three profiles, we have determined the thickness of the top and bottom Nb cladding layers to be 6.5 nm and 25.0 nm, respectively. The thickness of the carbon layer was found to be 30.7 nm. Table 1 summarizes the structural parameters of the Nb/C/Nb trilayer structure determined from the best fit results of measured Compton, elastic and fluorescence profiles. The structural parameters derived from scattering and fluorescence measurements were then used to fit the x-ray reflectivity profile, which was found to match closely with the measured reflectivity data (figure 7).

Figure 8 depicts the measured and fitted elastic and Mo Lα fluorescence profiles obtained from a Mo/Si multilayer structure in the vicinity of the first Bragg peak. From figures 8(a) and (b), it can be seen that the two profiles (elastic and Mo Lα fluorescence profiles) are very well correlated at the low and high angle sides of the Bragg peak. During the first Bragg reflection, an XSW field of periodicity of the multilayer period ($\Lambda = d$) is set up inside the multilayer structure (see inset of figure 1). At the low angle side of the Bragg peak, the antinodes of the XSW field remain in the low z layer. As the incidence angle advances across the Bragg region, these antinodes move towards the high z layer. At the high angle side of the Bragg peak, XSW antinodes completely coincide with the position of the high z layers. Because of this movement of XSW antinodes intensity,

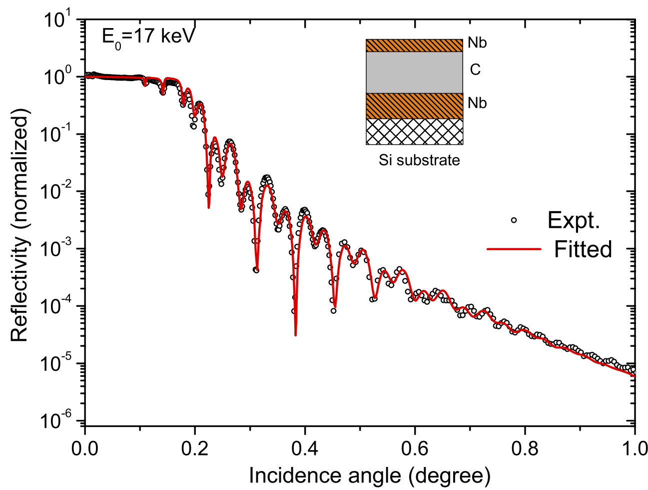

Figure 7. Measured XRR profile of Nb/C/Nb trilayer structure at incident x-ray energy of 17 keV. The scattered points show the experimental data while the solid line shows the fitted XRR profile using the structural parameters derived from the best fit results of elastic, Compton, and Nb Lα fluorescence measurements. The inset shows a schematic structure of the Nb/C/Nb trilayer structure.

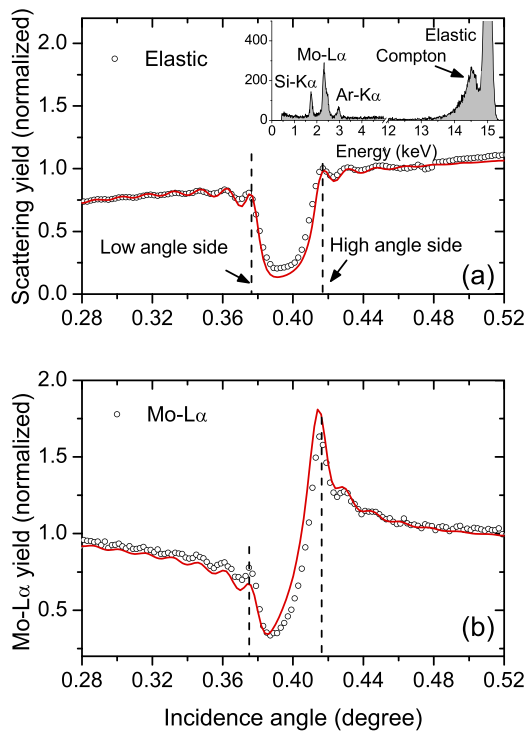

Figure 8. Measured and fitted elastic scattering and Mo Lα fluorescence profiles of a Mo/Si multilayer structure of parameters $d = 6.6$ nm, structure factor $(\Gamma) = 0.36$, $N = 20$ layer pairs. (a) Elastic scattering profile, and (b) Mo Lα fluorescence profile. The scattered points show the measured data while solid lines show the best fits to the experimental data. In the inset of (a), energy dispersive x-ray fluorescence spectrum of multilayer structure, measured at the Bragg angle ($\theta = 0.398°$) is shown.

the elastic scattering yield and Mo Lα fluorescence intensity are changed over the Bragg region. It can be seen from figures 8(a) and (b), at the high angle side of the Bragg peak, one obtains relatively higher elastic scattering yield and Mo Lα

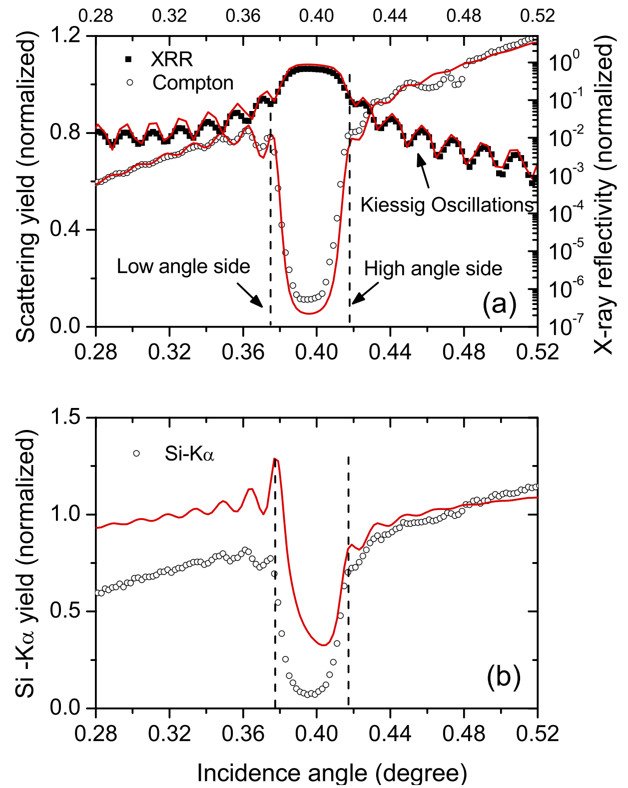

Figure 9. Measured and fitted Compton scattering and Si Kα fluorescence profiles of the Mo/Si multilayer structure. (a) Compton scattering profile, and (b) Si Kα fluorescence profile. It can be seen that at the low angle side of the Bragg peak, the measured Si Kα yield does not agree well with the calculated profile, obtained using the best results of elastic, Compton, and Mo Lα fluorescence profiles. In (a), we have also shown measured (solid scattered points) and fitted (solid line) XRR profiles of the multilayer in the vicinity of the first Bragg region.

fluorescence intensity compared to the low angle side. This occurs because at higher angle side of the Bragg peak the XSW antinodes exist in the high z layers, and therefore one observes an increased elastic scattering yield and fluorescence intensity from the Mo layers. In inset of figure 8(a), we have shown energy dispersive fluorescence spectrum Mo/Si multilayer structure recorded at the first Bragg angle ($\theta = 0.398°$). This figure clearly shows the presence the Si Kα, Mo Lα and Ar Kα (from air) fluorescence lines. Mo Lα line originates from the Mo layers while Si Kα peak appears from both Si layers and Si substrate. The Compton and elastic scattered peaks are also clearly distinguishable in this spectrum. The observed energy separation ($\sim$0.5 keV) between Compton and elastic scattered peaks was found to match with the calculated value assuming a scattering angle of 90° (detector angle).

Figure 9 shows the measured and fitted Compton and Si Kα florescence profiles obtained from the Mo/Si multilayer structure. Figure 9(a) shows the measured and fitted profiles for the Compton scattered intensity, while figure 9(b) shows the results for Si Kα fluorescence yield. In figure 9(a), we have also shown measured and fitted XRR profiles of the multilayer structure in the vicinity of the first Bragg region. By comparing these figures (cf figures 9(a) and (b)), it can be seen that the nature of the Compton and Si Kα fluorescence

profiles are more or less similar. At the low angle side of the Bragg peak, one observes relatively higher Compton and Si Kα fluorescence yields. This happens because the XSW antinodes exist in the low z layers, at the low angle side of the Bragg peak, and as a result the Compton scattered yield and Si Kα fluorescence intensity get enhanced from the Si layers.

From figures 8 and 9, it can be seen that the elastic and Compton scattering intensities across the Bragg region show a strong XSW oscillation as well as characteristic Kiessig oscillations at low and high angle side of the Bragg peak. By analyzing the two scattering profiles (Compton and elastic) in the vicinity of a Bragg region, it is possible to characterize the structural properties of the high z (Mo) and low z (Si) layers independently. Since the fluorescence emission from a low z layer is very inefficient consequently the XSW fluorescence profile of a low z layer is less sensitive to the structural properties of the layered medium, and sometimes it is quite difficult to fit the observed experimental profile. For example, in our case, for the Si Kα fluorescence profile (figure 9(b)), we could not achieve the best fit results close to the experimental data, even after employing the multilayer structure parameters derived from the best fit results of XRR, Mo Lα fluorescence, scattering measurements. For the Mo/Si multilayer, the best fit results obtained from the Compton and elastic scattering measurements give the thicknesses of Mo layer $\sim 2.48 \pm 0.05$ nm and Si layer $\sim 4.07 \pm 0.05$ nm. The roughness of Mo (Si) layers was found to be 0.3 nm (0.7 nm). These values were found to be in agreement with the results obtained from XRR and XSW fluorescence measurements of Mo Lα.

In comparison to conventional XSW fluorescence technique where analysis of the low z layers is a challenge, the present method provides the analysis for both high and low z layers independently. Moreover, the possibility of measuring several angle dependent signature profiles provides greater accuracy for the determination of microstructural parameters of a multilayer structure. The method also eliminates the requirement of using several excitation x-ray energies, close to the absorption edge of an element in order to obtain efficient fluorescence emission. A single excitation x-ray energy, well above the absorption edge of the high z element, can be used to record XSW assisted Compton and elastic profiles from a multilayer structure.

6. Conclusions

We have presented XSW enhanced elastic and Compton scattering measurements of thin layered materials. Scattered x-rays (Compton and elastic) emitted from the thin multilayer structures have been exploited to determine structural properties of both high and low z materials independently thereby facilitating complete characterization for thin layered materials. The applicability of the technique has been successfully demonstrated by applying it to few representative multilayer structures (Nb/C/Nb trilayer and Mo/Si periodic structures). It is interesting to note that the present approach greatly overcomes the limitation of the conventional XSW fluorescence technique and therefore is especially suitable for characterization of multilayer structures comprising of low z layers (e.g. Langmuir–Blodgett films, thin polymer or biological enzyme sensor films).

Acknowledgments

This work was carried out with the support of the Diamond Light Source Ltd UK. Technical support of A Malandain for the experiment setup is acknowledged. We are also grateful to M Nayak and G S Lodha for providing the multilayer samples.

References

[1] Spiller E 1972 *Appl. Phys. Lett.* **20** 365
[2] Barbee T W 1985 *Synthetic Modulated Structure Materials* (New York: Academic) p 313
[3] Windt D L, Donguy S, Hailey C J, Koglin J, Honkimaki V, Ziegler E, Christensen F E, Chen H, Harrison F A and Craig W W 2003 *Appl. Opt.* **42** 2415
[4] Wellock K, Theeuwen S J C H, Caro J, Gribov N N, van Gorkom R P, Radelaar S, Tichelaar F D, Hickey B J and Marrows C H 1999 *Phys. Rev.* B **60** 10291
[5] Costa A T Jr, de Castro Barbosa A C, d'Albuquerque e Castro J and Muniz R B 2001 *J. Phys.: Condens. Matter* **13** 1827
[6] Zahn P, Papanikolaou N, Erler F and Mertig I 2002 *Phys. Rev.* B **65** 134432
[7] Revaz B, Cyrille M C, Zink B L, Schuller I K and Hellman F 2002 *Phys. Rev.* B **65** 094417
[8] Parratt L G 1954 *Phys. Rev.* **95** 359
[9] Sinha S K, Sirota E B, Garoff S and Stanley H B 1988 *Phys. Rev.* B **38** 2297
[10] de Boer D K G 1991 *Phys. Rev.* B **44** 498
[11] Ghose S K and Dev B N 2001 *Phys. Rev.* B **63** 245409
[12] Krol A, Sher C J and Kao Y H 1988 *Phys. Rev.* B **38** 8579
[13] Kramer M, von Bohlen A, Sternemann C, Paulus M and Hergenrodera R 2006 *J. Anal. At. Spectrom.* **21** 1136
[14] Drakopoulos M, Zegenhagen J, Lee T L, Snigirev A, Snigireva I, Cimalla V and Ambacher O 2003 *J. Phys. D: Appl. Phys.* **36** A214
[15] Tiwari M K, Naik S R, Lodha G S and Nandedkar R V 2005 *Anal. Sci.* **21** 757
[16] Savage D E, Kleiner J, Schimke N, Phang Y-H, Jankowski T, Jacobs J, Kariotis R and Lagally M G 1991 *J. Appl. Phys.* **69** 1411
[17] Kortright J B 1991 *J. Appl. Phys.* **70** 3620
[18] Fullerton E E, Schuller I K, Vanderstraeten H and Bruynseraede Y 1992 *Phys. Rev.* B **45** 9292
[19] Salditt T, Metzger T H, Peisl J and Feidenhans R 1998 *J. Appl. Phys.* **83** 5179
[20] Kortright J B and Fischer-Colbrie A 1987 *J. Appl. Phys.* **61** 1130
[21] McMaster W H, Del Grande N K, Mallett J H and Hubbell J H 1969 Compilation of x-ray cross sections *Lawrence Livermore National Laboratory Report* UCRL-50174
[22] Hubbell J H, McMaster W H, Del Grande N K and Mallett J H 1974 X-ray cross sections and attenuation coefficients *International Tables for X-Ray Crystallography* vol 4, ed J A Ibers and W C Hamiliton (Birmingham: Kynoch Press) pp 47–70
[23] Sánchez del Río M and Dejus R J 1997 XOP: a multiplatform graphical user interface for synchrotron radiation spectral and optics calculations *Proc. SPIE* **3152** 148–57 (http://www.esrf.eu/computing/scientific/xop2.1/)
[24] http://csrri.iit.edu/periodic-table.html
[25] http://henke.lbl.gov/optical_constants/pert_form.html
[26] Sawhney K J S, Dolbnya I P, Tiwari M K, Alianelli L, Scott S M, Preece G M, Pedersen U K and Walton R D 2010 *AIP Proc. 10th Int. Conf. on Synchrotron Radiation Instrumentation 2009* at press
[27] Lodha G S 2009 *RRCAT News Lett.* **22** 7